Utilities detection through the sum of orthogonal polarization in 3D georadar surveys

Maurizio Lualdi* and Federico Lombardi

Dipartimento di Ingegneria Civile e Ambientale, Politecnico di Milano, Piazza Leonardo da Vinci 32, 20133 Milan, Italy

Received September 2013, revision accepted June 2014

INTRODUCTION

Ground penetrating radar (GPR) is a non-destructive technique that uses high frequency electromagnetic waves to locate shallow features in the subsurface. Traditional georadar utilizes short bursts of energy radiated into the ground and reflected back to detect electromagnetic discontinuities in the ground where there is a change in permittivity and conductivity (Daniels 2004).

Applications of this method have been expanded during the years to a wide variety of areas, such as environmental sensing (Seol *et al.* 2007; Knight 2001), landmine detection (Acheroy 2007; Lualdi and Zanzi 2005; Sato *et al.* 2004; Zanzi *et al.* 2002), archaeological investigations (Lualdi *et al.* 2006; Bonomo *et al.* 2013), geology (Beres *et al.* 1999; Saintenoy *et al.* 2013; Sénéchal *et al.* 2013) and civil engineering (Binda *et al.* 2004; Hugenschmidt *et al.* 2011; Donohue *et al.* 2011).

GPR has been intensely employed in detecting and locating underground utilities (Jeong *et al.* 2004) due to its high resolution imagery capability, fast data acquisition and cost effectiveness for mapping large areas (Birken *et al.* 2002; Simi *et al.* 2010). In this framework, damage to infrastructure during digging operations continues to be one of the major problems affecting the construction industry (McMahon *et al.* 2005; Thomas *et al.* 2009), therefore earlier detection of installed utilities gains more and more importance (Costello *et al.* 2007).

The challenge is to provide a clear and precise map in urban areas characterized by a high electromagnetic noise level, in terms of both target and surrounding soil properties.

From GPR theory, to guarantee a full reconstruction of the geometry of any target and to prevent spatial aliasing problems, it is necessary to acquire a dense and regular grid of traces (Lualdi *et al.* 2003; Yilmaz 2001). A three dimensional model of the site, in which a number of closely spaced bidimensional scans are connected in a predefined sequence, has the advantage of looking at the entire survey site at once with the possibility of following a target out of the 2D domain. This is especially important in areas with multiple intersecting or dipping targets (pipes, rebar, etc..) that may be hard to identify on single radar profiles (Bernstein *et al.* 2000).

For linear buried objects such as pipes and cables, the target is most clearly defined by recording the GPR survey lines at best angle to the orientation of the pipe (Daniels *et al.* 2003; Radzevicius and Daniels 2000; Roberts and Daniels 1996). To address this issue, numerous studies have exploited the relationship between GPR antenna configuration and target response

* maurizio.lualdi@polimi.it

regarding its physical and geometrical properties.

Major results have been obtained in the field of multicomponent GPR, in which data are recorded at multiple transmitter-receiver configurations: Streich and Van der Kruk (2007) and Van der Kruk *et al.* (2003) presented an imaging algorithm capable of correcting the radiation pattern and jointly migrating co-polarized and cross-polarized components; Böniger and Tronicke (2012) developed an attribute-based processing technique to extract and characterize buried pipes using orthogonal GPR data; Catapano *et al.* (2013) proposed a tomographic approach which considers the vectorial dependences for GPR 3D data inversion, providing an experimental evaluation of the improvements; Lehman *et al.* (2000) used co-pole data recorded with antennas oriented in mutually orthogonal directions to obtain a pseudo-scalar (circular) wavefield formulation, thus providing an overview of the benefits brought by their combination.

Another research field is the radar polarimetry analysis, in which the target scattering matrix features are employed to gain information on directivity attributes: Van Gestel and Stoffa (2001) applied the Alford rotation to extract the orientation of buried objects that have angle-dependent reflectivity; Villela and Romo (2013) exploited the invariant properties of the scattering matrix; Sassen and Everett (2009) employed the largest eigenvalue to compute a coherency-based algorithm; Chen *et al.* (2001) used eigenvalues and eigenvectors of the scattering matrix to find the orientation and aspect ratio of UXO-like targets.

These considerations underline the importance of conducting GPR surveys with two axially rotated measurements to avoid nulls over pipes and cables, when using linearly polarized co-pole antennas.

Wave propagation in anisotropic and heterogeneous media has a significant influence on the backscattered wavelet that is collected by the receiver antenna (Lampe and Holliger 2003; Giannopoulos and Diamanti 2008; Sena *et al.* 2005). Changes of polarization plane (Bliokh and Stepanovskii 2003; Renau *et al.* 1967), frequency dispersion (Cole and Cole 1941; Cassidy 2008; Lambot *et al.* 2005), spectral shift (Wunderlich and Rabbel 2013; Marcak and Gołębiowski 2008) and signal absorption (Bradford 2007; Van Dam 2002), just to list the main ones, have been noticed in commonly encountered soil textures. Strong contrast in dielectric properties that could occur in a layer-modelled subsurface deeply impacts on returning GPR signals as well (Arcone *et al.* 2003; Van der Kruk 2006).

Following this direction, it becomes ever more necessary to find a method to overcome these issues, in order to ensure target detection and provide unambiguous results.

Focusing on elongated target detection and reconstruction, this work proceeds along the direction of GPR data combination, introducing an approach based on the combination of mutually orthogonal GPR data to go beyond the antenna orientation effects. The validity of combining the two GPR 3D data volumes is demonstrated through an analysis of the obtained scattering matrix and with two field examples, which show the performances of the proposed method in different host media conditions. The first practical advantage is to have all buried targets in a single image, without the need of analysing separately two data volumes. Further on, improvements are expected in target continuity, signal to noise ratio enhancement and interpretability of the final GPR images.

THEORETICAL BACKGROUND

Scattering matrix formulation

Under the far field condition and the assumption of homogeneous soil (neglecting depolarization and dispersion effects), point heterogeneities in the subsurface can be represented by infinitesimal dipoles with moments parallel and proportional to the incident georadar wavefields (Balanis 1989). In case of elongated objects, the target is approximately a dipole antenna with equal geometrical characteristics.

The well-known scattering matrix, which represents a measure of the target response when illuminated by an arbitrary polarized wave, becomes therefore an index of the depolarization degree of the scattered wavefield. The time-domain matrix is defined as:

$$S(t) = \begin{bmatrix} S_{xx} & S_{xy} \\ S_{yx} & S_{yy} \end{bmatrix} \tag{1}$$

where the first subscript of the elements represents the transmitter direction and the second one corresponds to the receiver orientation.

Because of the reciprocity condition, the off-diagonal components are degenerated, so the matrix is Hermitian. The scattering characteristics can be obtained through the matrix decomposition: the eigenvectors represent the direction of the two axes of the polarization ellipse, while the eigenvalues quantify the target response when the antenna coordinate axis coincides with those of the target (first eigenvalue, principal scattering direction for metallic and low impedance pipes) and are at right angles to them (second one, principal scattering direction for high impedance dielectric pipes). For linear objects and co-pole configuration, the stronger eigenvalue gives the backscattered field when the longest dimension of the dipole is aligned with the target's principal axis (Radzevicius and Daniels 2000).

A rotation of the matrix in (1) is often employed for exploiting the responses variation associated with an alignment mismatch between sources and scatterers (Villela and Romo 2013; Chen *et al.* 2001). The rotated system is given by:

$$S^{\varphi} = RSR^{T}, \quad \text{where} \quad R = \begin{bmatrix} \cos\varphi & \sin\varphi \\ -\sin\varphi & \cos\varphi \end{bmatrix} \tag{2}$$

where φ represents the angular deviation from the alignment condition. The terms of the matrix S^{φ} become:

$$\begin{aligned} S^{\varphi}_{xx} &= S_{xx}\cos^2\varphi + S_{yy}\sin^2\varphi + \cos\varphi\sin\varphi(S_{xy} + S_{yx}) \\ S^{\varphi}_{yy} &= S_{xx}\sin^2\varphi + S_{yy}\cos^2\varphi - \cos\varphi\sin\varphi(S_{xy} + S_{yx}) \\ S^{\varphi}_{xy} &= S_{xy}\cos^2\varphi - S_{yx}\sin^2\varphi + \cos\varphi\sin\varphi(S_{yy} - S_{xx}) \\ S^{\varphi}_{yx} &= S_{yx}\cos^2\varphi - S_{xy}\sin^2\varphi - \cos\varphi\sin\varphi(S_{yy} - S_{xx}) \end{aligned} \tag{3}$$

For conductive cylindrical shape targets, scattering from an obliquely incident wave does not introduce additional components that are not present in the incident field (Balanis 1989). Therefore, when considering a co-pole antenna configuration emitting a linearly polarized wavefield, the term S_{xy} and S_{yx} in (1) and consequently in (3) is null.

To show the effect of combining mutually orthogonal data, we formulate the problem by adding the elements in (3) together with those in which the quantity (φ) is substituted with ($\varphi + 90°$). The superscript indicates the combination resulted element.

$$\begin{aligned} S_{xx}^{C} &= S_{xx}^{\varphi} + S_{xx}^{\varphi+90°} = S_{xx} + S_{yy} \\ S_{yy}^{C} &= S_{yy}^{\varphi} + S_{yy}^{\varphi+90°} = S_{xx} + S_{yy} \\ S_{xy}^{C} &= S_{xy}^{\varphi} + S_{xy}^{\varphi+90°} = 0 \\ S_{yx}^{C} &= S_{yx}^{\varphi} + S_{yx}^{\varphi+90°} = 0 \end{aligned} \tag{4}$$

The obtained scattering matrix thus becomes:

$$S^{C}(t) = \begin{bmatrix} S_{xx} + S_{yy} & 0 \\ 0 & S_{xx} + S_{yy} \end{bmatrix} \tag{5}$$

The eigenvalue decomposition of the product $\boldsymbol{S^C}(\boldsymbol{S^C})^T$, elements that represent the target backscattered magnitude and are index of the polarization state of the wavefield, leads to:

$$\begin{aligned} \left|\lambda_1^C\right|^2 &= \left|S_{xx} + S_{yy}\right|^2 \\ \left|\lambda_2^C\right|^2 &= \left|S_{xx} + S_{yy}\right|^2 \end{aligned} \tag{6}$$

The results in (5) and (6) lead to some significant considerations:

- The angular dependency in the preferred scattered directions (first elements of the obtained scattering matrix $\boldsymbol{S^C}$ in (5)) is removed.
- Both the diagonal elements in (5) include the two scattering directions, therefore the collected wavefield is unaffected from any deviation from the alignment condition, even from a complete polarization mismatch (dipole axis orthogonal to the maximum response configuration). This is evident also when considering the magnitude eigenvalue formulation.
- The equality between the two eigenvalues λ_1^C and λ_2^C in (6) means that the obtained wavefield has a circular footprint with no preferred scattering directions. A rotational invariant scattering matrix has been obtained.

For a visual comparison, Fig. 1a presents the polar representation of each element of the scattering matrix $\boldsymbol{S}$ in (1) versus the azimuth rotation (data are taken from registered GPR data).

From the diagram, it is clear that the amplitudes of the co-pole responses (respectively S_{xx} and S_{yy}) are quite the same except for a 90° angular shift, and each maximum value corresponds to the minimum of the orthogonal configuration. Fig. 1b depicts the elements of the combined matrix $\boldsymbol{S^C}$ formulated in (5). The effect of the combination is a variation of the polarization characteristics and the state of the backscattered wavefield as the antenna footprint assumes a circular shape, losing any azimuthal dependencies or alignment deviation relationship.

FIELD DATA EXAMPLES

Description and methodology

Two datasets are used to describe the performances of the algorithm. One taken across the *Geophysical Survey Systems, Inc.* test site (for a complete description see Roberts *et al.*, 2009) and the other acquired over a common road with known buried pipes mesh.

All the presented radar results have been processed using a tool developed by Politecnico di Milano running on *Mathworks* MATLAB software. Processing flows (Yilmaz, 2001) consisted of the following steps (Table 1):

The combination scheme consists of the algebraic sum of the data volume after the processing sequence. As they are linear operations, the steps applied to the data do not introduce any processing artifact.

To obtain an overall picture of the results, radar images are shown via depth slices obtained by plotting the amplitude of the brightest reflector over a specified depth range. The depth slices allow for a global comparison to be made between

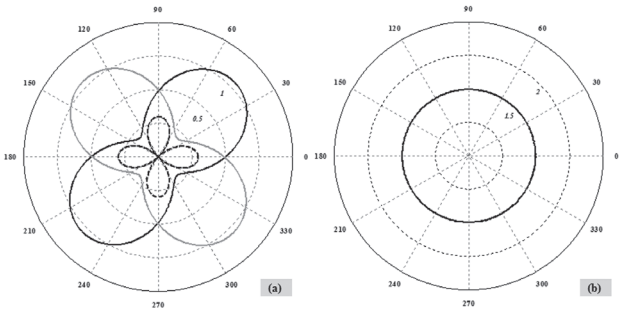

FIGURE 1

Polar diagrams showing the amplitude of the scattering matrix elements as a function of the angular deviation from the alignment condition. Co-pole elements S_{xx} and S_{yy} are the continuous black and grey lines, respectively, while the cross elements S_{xy} and S_{yx} are the black and grey dashed lines, respectively. (a) Single orientation wavefield footprint. (b) Combination of mutually orthogonal GPR data result. Note the circular shape assumed by the footprint.

TABLE 1

Processing steps and algorithm details.

Time calibration	Trace alignment	Frequency filtering	Velocity analysis	3D Migration	Data Envelope
Time shift	Correlation window	Zero-phase Butterworth filter.	Synthetic hyperbola fitting on real event.	2D-2step approach	Hilbert transform

images acquired using different survey configurations. Further on, all the presented images are displayed with the same amplitude range and contrasts setting, so each response can be properly compared.

Test 1: isotropic and homogeneous medium

The presented GPR data were collected using a 400 MHz antenna in co-pole configuration along two orthogonal directions. The acquisition procedure is illustrated in Fig. 2a. Markers on the ground and a rails system were used to obtain a precise matching between traces.

The investigated area, sketched in Fig. 2b including survey geometry, is composed of two metal pipes, one (marked A) oriented parallel to the crossline direction and the second (marked B) inclined at approximately 45°. Both targets are buried at a depth of 1 m and have a diameter of 10 cm. The host medium is homogeneous sand.

The acquisition parameters are listed in Table 2.

A medium velocity of 10 cm/s and a central wavelength of 25 cm lead to a radius to wavelength ratio of 0.2, which corresponds to a region of the backscattering width (Radzevicius and Daniels 2000) in which the perpendicular polarization (dipoles parallel to the longest axis of the target) almost doubles the orthogonal one.

The results of the perpendicular (0°) and parallel polarization (90°) are shown in Fig. 3a and 3b, respectively (antenna orientations are indicated in the upper corner). As the pipes' diameter and depth are equal, the differences in target imaging only apply to target/antenna orientation.

In both situations, the orientation mismatch between target and *GPR* dipole has a significant effect: focusing on Fig. 3a, one can clearly notice that the energy response of the inclined pipe (target B) is almost half of the aligned one (target A). The target is still visible, but it could be disguised by noise in a non-homogeneous situation. Despite a complete polarization mismatch, in Fig. 3b the pipe oriented along the crossline direction (target A) is still imaged, but it would be hardly identifiable without any hints as to its location: the target loses continuity and its energy content is hugely reduced. A possible reason for its presence could be the propagation in a homogeneous media, which cause the electromagnetical wavefield to lose some of the directional characteristics of the antenna pattern, approaching a wavefront closer to a spherical shape (Pramudita *et al.* 2009).

Figure 3c depicts the results of orthogonal data stacking. All the considerations made in the theoretical description are demonstrated and clearly evident: concerning the inclined target (target B), its energy level has been restored as the pipe and the GPR dipole were optimally configured, removing the contributed losses due to a drift from the alignment condition. This is clear if one evaluates the pixels amplitude of the two targets and compares them to those in Fig. 3a and 3b. Further on, both targets gain continuity in shape and reconstruction, thus reducing to zero the possibility of missing the target. The result is a rotational invariant image, as if the employed dipoles antenna had a circular footprint instead of a pronounced directivity feature. In other words, the resulting image is essentially an overlay of the different radar images that would be obtained with the most favourable survey geometry.

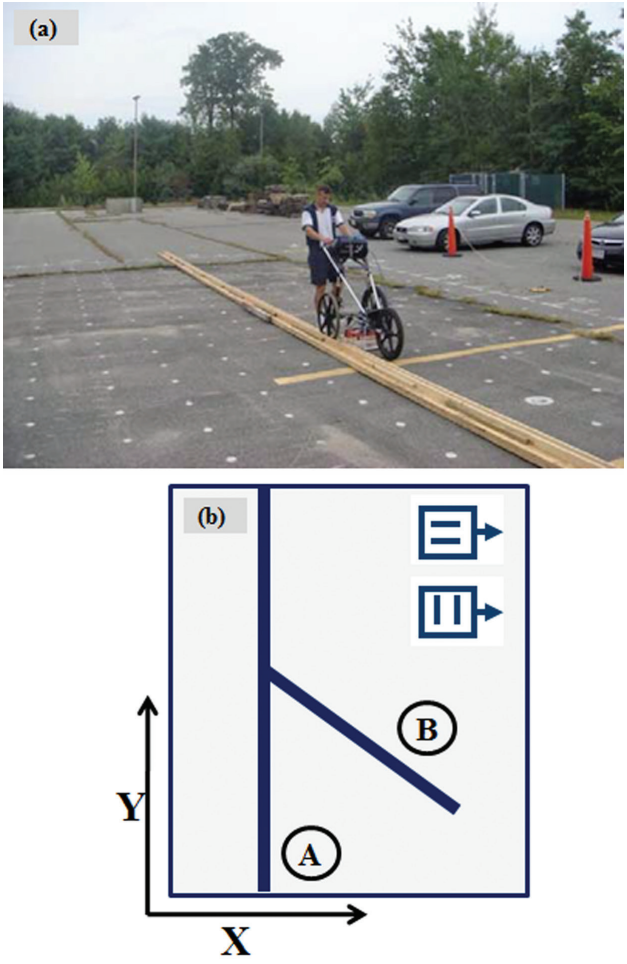

FIGURE 2

Test 1. (a) Data collection. (b) Schematic illustration of the investigated area and survey geometry. Host medium is homogeneous sand.

TABLE 2

Test 1, acquisition parameters.

Inline sampling (Δx)	Crossline sampling (Δy)	Time sampling (Δt)	Time window	Acquisition time
1.25 cm controlled by wheel odometer (decimated to 5 cm in post processing).	5 cm controlled by rail system and markers.	0.09 ns	50 ns	4 hours for each survey

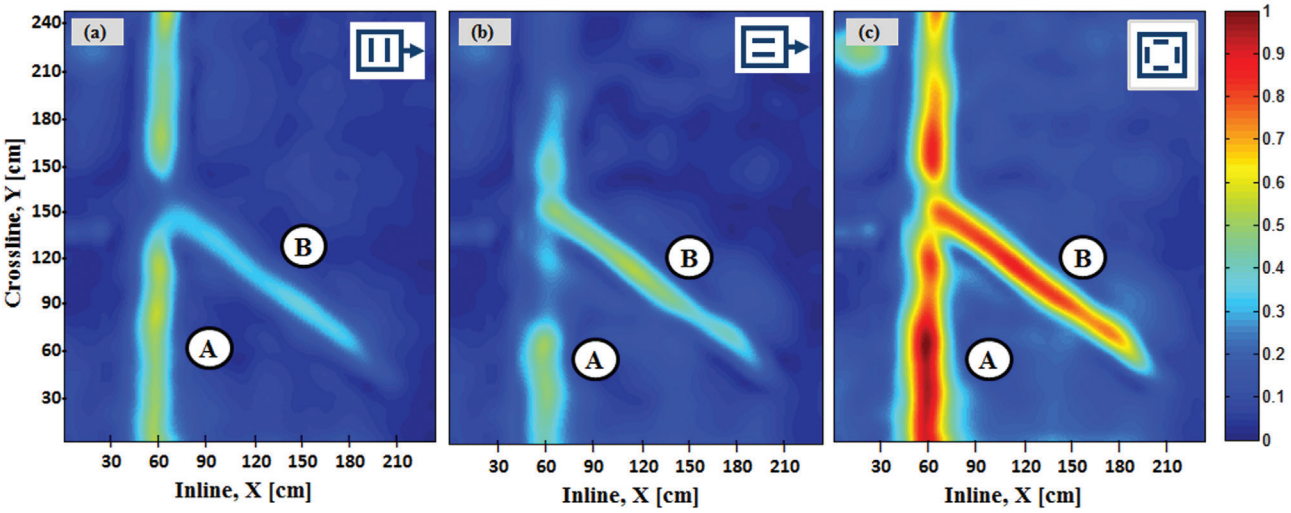

FIGURE 3

Test 1, radar depth slices. Depth 1 metre, thickness 15 cm. (a) Orientation 0°. (b) Orientation 90°. (c) Stack of the two orthogonal cubes. All the depth slices are plotted using equal amplitude scaling.

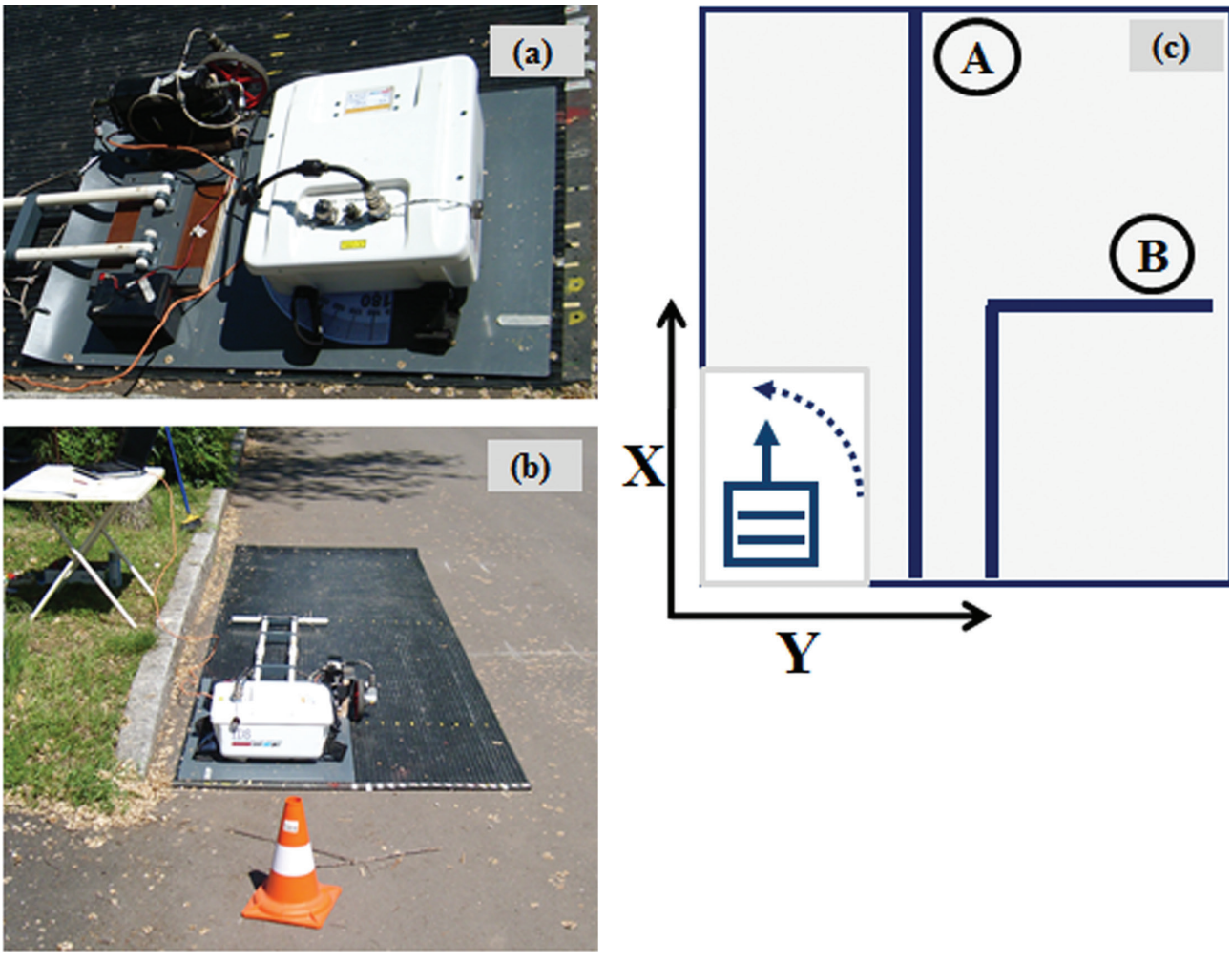

FIGURE 4

Test 2. (a) Georadar equipment and rotational device. (b) Georadar and PSG setup. (c) Schematic illustration of the investigated area and survey geometry.

TABLE 3
Test 2, acquisition parameters.

Inline sampling (Δx)	Crossline sampling (Δy)	Time sampling (Δt)	Time window	Acquisition time
4 cm controlled by wheel odometer	4 cm controlled by the PSG.	0.11 ns	30 ns	45 minutes for each survey

Test 2: anisotropic and heterogeneous medium

This dataset was acquired over a street in Busto Arsizio, northern Italy, characterized by a known subsurface utilities mesh, in order to test the performance of the algorithm in a real urban environment.

An *IDS* (Ingegneria dei Sistemi, Italy) dual-frequency antenna was used, with central frequencies of 200 and 600 MHz, in co-pole configuration. Two pairs of orthogonal azimuths were collected, *i.e.* 0° (parallel, referring to the previous section convention), 90° (perpendicular), 30° and 120°. Dipole rotation was achieved with a protractor device placed just under the CMP of the antennas (Fig. 4a). Inline movements were controlled through PSG (Pad System for Georadar, U.S. Patent no. US 7,199,748 B2 of Politecnico di Milano, Italy, in Lualdi *et al.* (2006) and Lualdi (2011)), as illustrated in Fig. 4b.

The investigated area, sketched in Fig. 4c, consists of two pipes: a water filled PVC pipe (marked A) aligned with the inline direction, with a diameter of 6 cm, and a metallic one (marked B) with a traverse shape and a diameter of 8 cm.

The host medium is expected to be quite heterogeneous, as a result of different restoration and maintenance operations that may have been performed during the years. The pipes are buried at a depth of approximately 70 cm.

The configuration parameters for the 600 MHz antenna are described in Table 3.

In this case the velocity was approximately 13 cm/ns, which resulted in a central wavelength of 22 cm. For the metal pipes, the radius to wavelength ratio is 0.18 and the same considerations made for the previous experiments still hold. Reasonably considering the water filled pipe as a conductive target, its ratio of 0.13 belongs to a region in which the interval between the two orthogonal polarizations is not so wide.

Figures 5a to 5d show the final image of the single orientation acquisition (the survey angle is sketched at the top corner of each picture). Differences compared to the previous case (Test 1) are evident. The heterogeneity of the surrounding soil makes the target lose its full reconstruction and energy balancing, as a consequence of the anisotropy effect on amplitude and phase of the backscattered wavelet.

From Fig. 5a to 5d, the following features could be underlined:

- Target discontinuity, due in part to heat conversion and to the unconsolidated near-surface that absorbs higher frequency energy more than the underlying compact layers. Waveguide dispersion should be taken into account as well (previous heavy rainfall events recorded in the area).

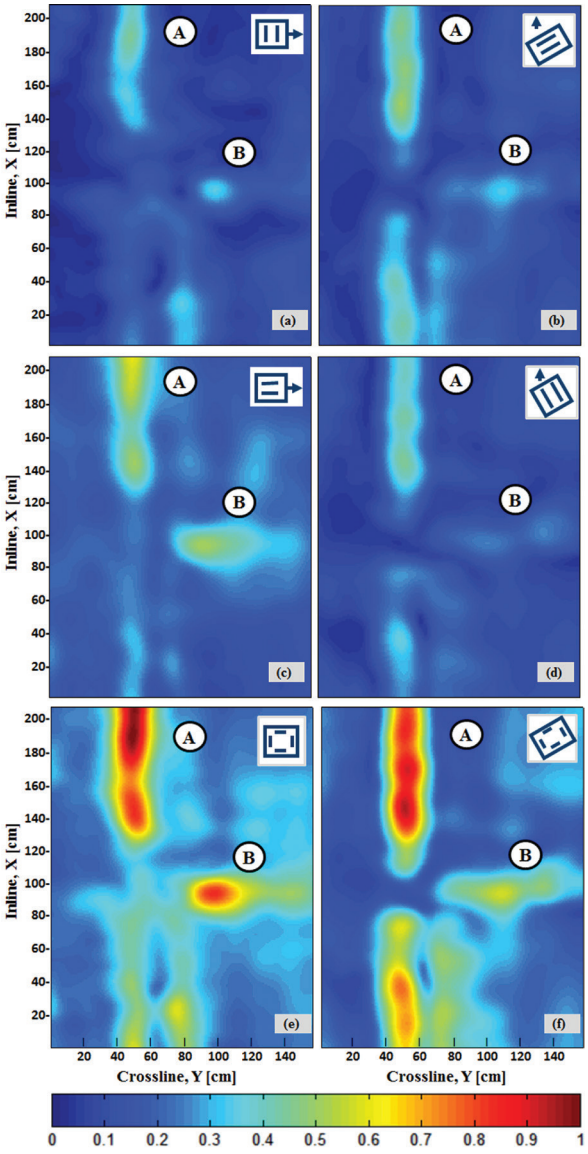

FIGURE 5
Test 2, radar depth slices. Depth 70 cm, thickness 10 cm. (a) Orientation 0°. (b) Orientation 30°. (c) Orientation 90°. (d) Orientation 120°. (e) Aligned stack, 0° and 90° (aligned stack). (f) Inclined stack, 30° and 120°. All the depth slices are plotted using equal amplitude scaling.

- Vanishing of polarization signatures, because of the changes in polarization plane that occur during propagation in irregular and inhomogeneous layers. Multiple scattering events are the most probable cause of depolarization.

The pipes mesh is hardly detectable (Fig. 5b and 5c) or even misleading (Fig. 5a and 5d). The propagation phenomena have a significant impact on the interpretability of the images: target continuity is missed and none of the four different orientations are capable of providing an unambiguous image of the subsurface.

These small-scale changes impact directly on the problem formulation, as evident in Fig. 5e (0° and 90°, namely aligned combination) and 5f (30° and 120°, namely inclined combination). The stack of mutually orthogonal GPR data is not able to recover the spreading energy and reach the optimal geometry condition. Note that changes in polarization state could invalidate the hypothesis of data orthogonality or introduce random cross-components that are not collected at the receiver, while absorption and dispersion phenomena are very likely to irregularly damp down the amplitude of the wave.

Despite a lower quality compared to the case presented in Test 1, the proposed algorithm still brings significant improvements (Fig. 5e and 5f): the SNR ratio is enhanced and the target reconstruction is facilitated. Target continuity is hugely improved, especially for the horizontal stroke of the L-shape target (target B) that could be easily connected to its follow-up part. When comparing the two stacking results, it can be noticed that the aligned combination (0° and 90°, Fig. 5e) gets finer results. Concerning the PVC pipe (target A), the propagation is such that both stacks are not able to recover the amplitude decay. This is more evident in the combination of the inclined data (30° and 120°, Fig. 5f), where the target reconstruction is abruptly interrupted. Also in this case, the combination of the parallel and perpendicular data shows better results.

As the model states (Theoretical background section) that the results should be independent from the choice of the first angle, the different results mean that the soil anisotropy deeply influences the inner formulation of the problem. The fact that better results are obtained with the sum of the data volumes acquired at the best angle towards the pipes (0° and 90°, Fig. 5e) are a further consequence: drifting away from the best configuration causes propagation phenomena to overwhelm the recovery brought by the combination. Differences in MultiPolarization results can be noticed in Fig. 5e and 5f (stacked orientation are sketched in the upper corner).

In the case of anisotropy and heterogeneity of the surrounding soil, this approach acts as an azimuthal data stacking process, providing different views of the same situation in order to globally improve the imaging performances. The signal to noise ratio is enhanced thus target reconstruction can be performed more easily and with lower failure risk.

CONCLUSIONS AND PERSPECTIVES

In a framework of urban underground networks assessment, an innovative approach to ensure target detection and reconstruction through 3D georadar surveys has been described and tested. Two of the major concerns that exist about the technique have been faced: the impact of survey geometry on target response and alteration of the wave due to soil texture variation. The approach is based on the combination of GPR data acquired along orthogonal directions, which should remove any angular dependency from the final radar images making the target scattering matrix an invariant feature. This property enables us to overcome the polarization issues that exist for linear targets.

GPR results show varying performances according to the surrounding media conditions. When wave propagation is not affected by strong variations in dielectric and conductivity properties or multiple scattering, the stack of the two data volumes brings significant improvement. The final images reach a very high level of clarity thanks to better target reconstruction and energy recovery. As far as inclined pipes are concerned, on which the effect is especially remarkable, the stack result is closely similar to an image that would be obtained with the optimal antenna-target alignment. In addition, there is the practical advantage for the on field end user of having all the buried targets in a single frame.

The test performed in more realistic urban conditions suffers from the anisotropy and heterogeneity of the terrain. Therefore, the dual azimuth approach required by scattering theory is no longer enough, because of the significant modifications that propagation introduces in the wavelet characteristics. These small-scale abrupt variations can not be taken into account for a generalized model, but need to be exploited in a more systematic way. Results show that the strategy still brings huge improvement, particularly concerning target reconstruction and pipes mesh identification. Images are clearly more understandable and noiseless than the single azimuth one. The amplitude and phase alteration of the wavelet reduces the hypothesis of orthogonality between volumes, so the stack could not achieve a complete energy recovery. Another consequence is the difference in target imaging between the results coming from the two pairs of perpendicular data volume stack. In the worst case scenario, the multiazimuth strategies would act like a stack of different views of the object, enhancing the signal to noise ratio rather than recovering the polarization mismatch losses.

In light of these considerations, the described MultiPolarization strategy has revealed a remarkable potential for linear target detection, overtaking the polarization signatures in the case of homogeneous soil conditions, and also mitigating the impact of wavelet alteration in strong varying media.

ACKNOWLEDGEMENTS

This work was supported by Politecnico di Milano under project 5 per mille. Authors would like to thank *Geophysical Survey Systems, Inc.* for the provisioning of the dataset and *Sintec 3D* for supplying georadar equipment used for the Busto Arsizio experiment.

REFERENCES

Acheroy M. 2007. Mine action: status of sensor technology for close-in and remote detection of anti-personnel mines. *Near Surface Geophysics* **5**, 43–55.

Arcone S.A., Peapples P.R. and Liu L.2003. Propagation of a ground-penetrating radar (GPR) pulse in a thin-surface waveguide. *Geophysics* **68**, 1922–2933.

Balanis C.A. 1989. *Advanced Engineering Electromagnetics*, 1st ed. New York: Wiley & Sons, 1989.

Beres M., Huggenberger P., Green A.G. and Horstmeyer H. 1999. Using two- and three-dimensional georadar methods to characterize glacio-fluvial architecture. *Sedimentary Geology* **129**, 1–24.

Bernstein R., Oristaglio M., Miller D.E. and Haldorsen J. 2000. Imaging radar maps underground objects in 3-D. *IEEE Computer Application in Power* **13**, 20–24.

Binda L., Zanzi L., Lualdi M. and Condoleo P. 2004. The use of georadar to assess damage to a masonry Bell Tower in Cremona Italy. *NDT&E International* **38**, 171–179.

Birken R., Miller D.E., Burns M., Albats P., Casadonte R., Deming R. *et al*. 2002. Efficient large scale underground utility mapping with a multi-channel ground penetrating imaging radar system. *Proceeding of SPIE **4758**, 9th International Conference on Ground Penetrating Radar*, 186.

Bliokh K.Yu. and Stepanovskii Yu.P. 2003. On the change in electromagnetic wave polarization in a smooth one-dimensionally inhomogeneous medium. *Journal of Experimental and Theoretical Physics* **97**, 479–484.

Böniger U. and Tronicke J. 2012. Subsurface Utility Extraction and Characterization: Combining GPR Symmetry and Polarization Attributes. *IEEE Transaction on Geoscience and Remote Sensing* **50**, 736–746.

Bonomo N., Osella A. and Ratto N. 2013. GPR investigations at an Inca-Spanish site in Argentina. *Near Surface Geophysics* **11**, 449–456.

Bradford J.H. 2007. Frequency-Dependent Attenuation Analysis of Ground-Penetrating Radar Data. *Geophysics* **72**, J7–J16.

Cassidy N.J. 2008. Frequency-dependent attenuation and velocity characteristics of nano-to-micro scale, lossy, magnetite-rich materials. *Near Surface Geophysics* **6**, 341–354.

Catapano I., Affinito A., Gennarelli G., Di Maio F., Loperte A. and Soldovieri F. 2013. Full-three-dimensional imaging via ground penetrating radar: assessment in controlled conditions and on field for archaeological prospecting. *Applied Physics A: Materials Science and Processing*, 2013

Chen C.C., Higgins M.B., O'Neill K. and Detsch R. 2001. Ultrawide-bandwidth fully-polarimetric ground penetrating radar classification of subsurface unexploded ordnance. *IEEE Transactions on Geoscience and Remote Sensing* **39**, 1221–1230.

Cole K.S. and Cole R.H., 1941. Dispersion and absorption in Dielectrics. *Journal of Chemical Physics* **9**, 341–351.

Costello S.B., Chapman D.N., Rogers C.D.F. and Metje N. 2007. Underground asset location and condition assessment technologies. *Tunneling and Underground Space Technology* **22**, 524–542.

Daniels D.J. 2004. *Ground Penetrating Radar*, 2nd edn. Peter Peregrinus Ltd., London, U.K.

Daniels J.J., Wielopolski L., Radzevicius S. and Bookshar J. 2003. 3D GPR Polarization Analysis for Imaging Complex Objects. *Symposium on the Application of Geophysics to Engineering and Environmental Problem*, 585–597.

Donohue S., Gavin K. and Tolooiyan A. 2011. Geophysical and geotechnical assessment of a railway embankment failure. *Near Surface Geophysics* **9**, 33–44.

Giannopoulos A. and Diamanti N. 2008. Numerical modeling of ground penetrating radar response from rough subsurface interfaces. *Near Surface Geophysics* **6**, 357–369.

Hugenschmidt J., Kasa C. and Kato H. 2011. GPR for the Inspection of Industrial Railway Tracks. *Near Surface 2011, 17th European Meeting of Environmental and Engineering Geophysics*, Leicester, United Kingdom.

Jeong H.S., Abraham D.M. and Lew J.J. 2004. Evaluation of an Emerging Market in Subsurface Utility Engineering. *Journal of Construction Engineering Management* **130**, 225–234.

Knight R. 2001. Ground penetrating radar for environmental applications. *Annual Review of Earth and Planet Science* **29**, 229–255.

Lambot S., Van den Bosch I., Stockbroeckx B., Druyts P., Vanclooster M. and Slob E. 2005. Frequency dependence of the soil electromagnetic properties derived from ground penetrating radar signal inversion. *Subsurface Sensing Technology and Application* **6**, 73–87.

Lampe B. and Holliger K. 2003. Effects of fractal fluctuations in topographic relief, permittivity and conductivity on ground-penetrating radar antenna radiation. *Geophysics* **68**, 1934–1944.

Lehmann F., Boerner D., Holliger K. and Green A. 2000. Multicomponent georadar data: Some important implications for data acquisition and processing. *Geophysics* **65**, 1542–1552.

Lualdi M. 2011. True 3D Acquisition using GPR over small areas: A cost effective solution. *Proceeding of the Symposium on the Application of Geophysics to Engineering and Environ. Problems*, SAGEEP, 541–550.

Lualdi M. and Zanzi L. 2005. Testing a safe acquisition procedure for an effective application of GPR to security operations. *Proceeding of the Symposium on the Application of Geophysics to Engineering and Environ. Problems*, SAGEEP, 613–623.

Lualdi M., Zanzi L. and Binda L. 2003. Acquisition and processing requirements for high quality 3D reconstructions from GPR investigations. *Proceeding of the International Symposium Non Destructive Testing in Civil Engineering NDT-CE*.

Lualdi M., Zanzi L. and Sosio G. 2006. A 3D GPR survey methodology for archeological applications. *11th International Conference on Ground Penetrating Radar* **9**.

Lualdi M., Zanzi L., Ciano M., Marchesini P. and Carsana M. 2006. PSG (Pad System for Georadar), a new positioning system to perform 3D georadar investigations for utility mapping. *24th No-Dig International Conference and Exhibition, Australasian Society for Trenchless Technology*, 514–520.

Marcak H. and Gołębiowski T. 2008. Changes of GPR spectra due to the presence of hydrocarbon contamination in the ground. *Acta Geophysica* **56**, 485–504.

McMahon W., Burtwell M.H. and Evans M. 2005. Minimizing street works disruption: the real costs of street works to the utility industry and society. UKWIR report 05/WM/12/8. UK Water Industrial Research, London.

Pramudita A.A., Kurniawan A., Suksmono A.B. and Lestari A.A. 2009. Effect of antenna dimensions on the antenna footprint in ground penetrating radar applications. *Microwaves, Antenna & Propagation*, IET **3**, 1271–1278.

Radzevicius S.J. and Daniels J.J. 2000. Ground penetrating radar polarization and scattering from cylinders. *Journal of Applied Geophysics* **45**, 111–125.

Renau J., Cheo P.K. and Cooper H.G. 1967. Depolarization of Linearly Polarized EM Waves Backscattered from Rough Metals and Inhomogeneous Dielectrics. *Journal of Optical Society of America* **57**, 459–461.

Roberts R., Cist D. and Kathage A. 2009. Full-resolution GPR imaging applied to utility surveying: insights from multi-polarization data obtained over a test pit. *IWAGPR 2009*, Granada, Spain, 126–131.

Roberts R.L. and Daniels J.J. 1996. Analysis of GPR polarization phenomena. *Journal of Environmental Engineering Geophysics* **1**, 139–157.

Saintenoy A., Friedt J.-M., Booth A.D., Tolle F., Bernard E., Laffly D. *et al*. 2013. Deriving ice thickness, glacier volume and bedrock morphology of Austre Lovénbreen (Svalbard) using GPR. *Near Surface Geophysics* **11**, 253–261.

Sassen D.S. and Everett M.E. 2009. 3D polarimetric GPR coherency attributes and fullwaveform inversion of transmission data for characterizing fractured rock. *Geophysics* **74**, J23–J34.

Sato M., Hamada Y., Feng X., Kong F.-N., Zeng Z. and Fang G. 2004. GPR using an array antenna for landmine detection. *Near Surface Geophysics* **2**, 7–13.

Sénéchal G., Rousset D. and Gaffet S. 2013. Ground-penetrating radar investigation inside a karstified limestone reservoir. *Near Surface Geophysics* **11**, 283–291.

Sena A.R., Stoffa P.L and Sen M.K. 2005. Migration of Ground Penetrating Radar in heterogeneous and dispersive media. New strategies for European remote sensing. *Proceedings of the 24th Symposium of the European Association of Remote Sensing Laboratories*, Dubrovnik, Croatia.

Seol S.J., Yokota T., Mitsuhata Y., Kwon H.-S. and Uchida T. 2007. Application of ground-penetrating radar in detecting water leakage from artificial sandy ground. *Near Surface Geophysics* **5**, 301–308.

Simi A., Manacorda G., Miniati M., Bracciali S. and Buonaccorsi A. 2010. Underground asset mapping with dual-frequency dual-polarized GPR massive array. *13th International Conference on Ground Penetrating Radar (GPR 2010)*, 1–5.

Streich R. and Van der Kruk J. 2007. Accurate Imaging of Multicomponent GPR Data Based on Exact Radiation Patterns. *IEEE Transactions Geoscience and Remote Sensing* **45**, 93–103.

Thomas A.M., Rogers C.D.F., Chapman D.N., Metje N. and Castle J. 2009. Stakeholder needs for ground penetrating radar utility location. *Journal of Applied Geophysics* **67**, 345–351.

Van Dam R.L. 2002. Iron oxides as a cause of GPR reflections. *Geophysics* **67**, 536–545.

Van der Kruk J. 2006. Properties of Surface Waveguide derived from Inversion of Fundamental and Higher Mode Dispersive GPR Data. *IEEE Transactions on Geoscience and Remote Sensing* **44**, 2908–2915.

Van der Kruk J., Wapenaar C.P.A., Fokkema J.T. and Van den Berg P.M. 2003. Three-dimensional imaging of multicomponent ground penetrating radar data. *Geophysics* **68**, 1241–1254.

Van Gestel J.P. and Stoffa P.L. 2001. Application of Alford rotation to ground-penetrating radar data. *Geophysics* **66**, 1781–1792.

Villela A. and Romo J.M. 2013. Invariant properties and rotation transformations of the GPR scattering matrix. *Journal of Applied Geophysics* **90**, 71–81.

Wunderlich T. and Rabbel W. 2013. Absorption and frequency shift of GPR signals in sandy and silty soils: empirical relations between quality factor Q, complex permittivity and clay and water contents. *Near Surface Geophysics* **11**, 117–127.

Yilmaz O. 2001. *Seismic Data Analysis*, 2nd ed. Society of Exploration Geophysicists, Tulsa, US.

Zanzi L., Lualdi M., Braun H.M., Borisch W. and Triltzsch G. 2002. An ultra high frequency radar sensor for humanitarian demining tested on different scenarios in 3D imaging mode. *9th International Conference on Ground Penetrating Radar*, 240–245.